

Fock-Darwin states in a circular n-p junction of topological surface states

Jun Zhang, Ye-ping Jiang*

Key Laboratory of Polar Materials and Devices (MOE) and Department of Electronics, East China Normal University, Shanghai 200241, China

We analyze and observe the Fock-Darwin (FD) states in a circular n-p junction (CNPJ) of topological surface states. Theoretically, in the CNPJ induced by the sub-surface point charge, the FD states of Dirac fermions are found to have a unique core-shell structure of trapped electrons and holes. The interplay between them is highly tunable by the magnetic field, which has no analog in their conventional counterparts and even in FD states of Dirac fermions confined by the most-studied parabolic-like potentials. A modified Einstein–Brillouin–Keller method is introduced to derive the electron-core states semiclassically. Experimentally, we obtain the clearly resolved FD states of topological surface states up to 14 Tesla which are very different from those of conventional electrons. Our data also visualizes directly the field-dependent potential landscape that may be modified by the electron-electron interactions in a CNPJ at the surface of a three-dimensional topological insulator thin film. Our findings signal the high tunability of the FD states of topological surface states in CNPJs that can be obtained by molecular beam epitaxy.

PACS numbers: 73.20.-r, 68.37.Ef, 73.21.-b, 73.50.Gr

* Corresponding authors. Email: ypjiang@clpm.ecnu.edu.cn

I. INTRODUCTION

The surface of a three-dimensional (3D) topological insulator (TI) [1,2] hosts a two-dimensional (2D) Dirac electron system with photon-like dispersion and a spin-momentum helicity, embedding a nontrivial Berry phase of π . When the Fermi level is tuned close to the Dirac point, the potential variations lead to features such as p-n or n-p-n junctions that strongly affect the propagation of Dirac electrons by acting as focusing or lensing mechanisms [3,4], rendering these systems as ideal platforms to develop quantum electron optics. In addition, despite the fact that the Dirac electrons cannot be confined completely by electrostatic approach due to Klein tunneling [5,6], they can be trapped by a circular n-p junction (CNPJ) [7-11]. The n-p junctions can act as mirrors for Dirac electrons with large incident angles [12]. In TIs, by depleting the bulk carriers carefully and introducing sub-surface charged defects, a surface full of electron puddles in the slightly p-doped background has been reported [7]. These puddles are near-circular n-p junctions that can trap the Dirac electrons efficiently.

In quantum dots of conventional electron systems, the confined states, showing electronic structures that mimic the atomic levels [7], are known as the Fock-Darwin (FD) states or artificial atoms [13,14]. Unlike the conventional ones, we show both semiclassically and numerically that the quasi-confined TI surface states (SS) in a CNPJ have a unique electron and hole (e-h) core-shell structure, the Klein tunneling between which can be effectively tuned by the magnetic field. These behaviors are unique to FD states in the CNPJ induced by sub-surface point charge, which introduces a potential profile different from the parabolic-like ones [14]. We model the interplay between the electron-core and the hole-shell by an additional phase term coming from the Klein tunneling between them. This leads to a modified Einstein–Brillouin–Keller (EBK) method to derive semiclassically the electron-core states that match well with the numerical results as well as the experimental data. Experimentally, we observe clearly resolved electron-core states evolving from the electrostatic-confined region to the Landau region in a CNPJ of TI SS on the surface of a 7-QL Sb_2Te_3 film, which is near the thickness limit of this 3D TI [15].

II. THE E-H CORE-SHELL STRUCTURE AND THEIR INTERPLAY IN A

CNPJ OF TISS

In our experiment, the CNPJ is a near-circular electron-puddle (~ 100 nm in width) induced by sub-surface charged defects in the slightly p-doped 7-QL Sb_2Te_3 film [detailed in Appendix A], in which case the confining potential follows the typical screened potential of defects $U(\mathbf{r}) = \mu_0 e^{-|\mathbf{r}|^2} + \mu_\infty$. Here $\mu_0 + \mu_\infty$ and μ_∞ define the Dirac energy in the CNPJ center and that of the p-doped back ground. Different from the most-studied parabolic-like ones, the potential is nearly flat away from the junction center. We see that in the following this kind of potential profile leads to an e-h core-shell structure of the FD states in the CNPJ.

In the magnetic field, the Dirac Hamiltonian for the surface state electrons in the confining potential is $\varepsilon\psi(\mathbf{r}) = [v_F\boldsymbol{\sigma} \cdot \mathbf{p} + U(\mathbf{r})]\psi(\mathbf{r})$, where $\mathbf{p} = \mathbf{q} + e\mathbf{A}$. Here \mathbf{p} , \mathbf{q} , \mathbf{A} are canonical momentum, kinetic momentum and the magnetic vector potential. In the symmetric gauge and circular symmetric potential, \mathbf{p} and \mathbf{q} are given by

$$\begin{aligned} q_r = p_r &= \pm\sqrt{(\varepsilon - U)^2 - (m/r - Br/2)^2}, \\ q_\theta = p_\theta - A_\theta &= m/r - Br/2, \end{aligned} \quad (1)$$

where ε , U , r , B , are in units of ε^* , r^* , B^* as described in the caption of Fig. 1.

From q_r we see that the conditions $\varepsilon \geq E_1(r) = U + |m/r - Br/2|$ and $\varepsilon \leq E_2(r) = U - |m/r - Br/2|$ defines the classically allowed regions for electron and hole states, respectively. Fig. 1(a) shows these two regions (shadowed) for $m = 7/2$ states at 0 T. Here $q_r = 0$ gives the classical turning points r'_i , r_i , r_o , r'_o for the electrons' and holes' trajectories (hollow dots in Figs. 1, 2, 3). The second term beneath the root sign of q_r , that is, the kinetic angular momentum, $q_\theta = m/r - Br/2$ determines the barrier width $d = r_o - r_i$, which increases with the angular momentum m at zero magnetic field similar to the planar-junction case [12]. This leads to a gap (the classically forbidden region, un-shadowed in Fig. 1(a)) centered around the potential profile. This gap becomes smaller for the states with smaller m (see Appendix C for the $m = 1/2$ states), recalling that m acts as the tunneling barrier for trapped states.

An e-h core-shell structure is thus formed in the CNPJ. Figure 1(a) also displays the radial distribution of local partial density of states (LPDOS, numerical as described in

the Appendix B) for the $(0, 7/2)$ state, which is found to be composed of both electron and hole states that couple strongly with each other (see the appreciable LPDOS in the gap region). In addition, at zero magnetic field the hole shell is delocalized.

The FD states composed of an electron-core and a hole-shell in the CNPJ defined by $U(\mathbf{r})$ become fully localized in the presence of an arbitrary small magnetic field. The hole-shell states also become quantized in this case. Furthermore, there appears a touch point between the electron-core and hole-shell (Fig. 1(b)). This critical point, denoted by (ε_c, B_c) , sits on the potential profile (n-p boundary) and moves down in energy with the increasing magnetic field. Here (ε_c, B_c) satisfies $B_c = 2m / \ln(\mu_0/\varepsilon_c - \mu_\infty)$ and is derived from the condition of $q_r = q_\theta = 0$, in which case the electron approaches the n-p junction perpendicularly. A perpendicular incident angle leads to the total transmission in the Klein tunneling case of Dirac fermions, rendering a zero-gap situation defined as the critical point. Figure 1(c) shows the classical orbits of $(0, 7/2)$ along with the 3D view of the e-h core-shell structure (blue and red) at 1 T. Figure 1(d) is the corresponding trajectories in the momentum-energy space along the radial coordinate. For Dirac electrons, the cyclotron orbits winding around the Dirac point acquire an additional phase of π in the massless case [7]. Here the $(0, 7/2)$ state lies below the critical point. The Berry-phase of electron and hole states $(\varphi_B^e, \varphi_B^h)$ for $(0, 7/2)$ is $(0, 1)$ (in units of π). Actually the critical point defines the critical condition for states (for both electrons and holes) with momentum m to switch the Berry phase [7]. Increasing the energy or magnetic field through the critical condition leads to the Berry-phase switch of electron and hole states $(\varphi_B^e, \varphi_B^h)$ from $(0, 1)$ to $(1, 0)$.

III. THE MODIFIED EBK CONDITION FOR THE ELECTRON CORE

Figures 2(a) and 2(b) show the radial LPDOS ($m = 7/2$, numerical) as well as the spatial distribution of the state $(0, 7/2)$ at 0 T and 1 T, respectively. The e-h core-shell structures obtained numerically match well with the semiclassical ones. Near the critical point the forbidden region shrinks. The trapped electron and hole states are strongly coupled in such case, leading to the strong broadening in LPDOS for the states near the critical point (Fig. 1(b)). The trapped electron states of $(1, 7/2)$ and $(2, 7/2)$ that are in close approximate to the critical condition become nearly undiscernible. For $(0,$

7/2), the trapped electron is separated from the hole continuum by a barrier of width $d \sim 17$ nm with a tunneling probability of $t \sim 0.31$ at 0 T, while $d \sim 6$ nm and $t \sim 0.83$ at 1 T. Here the tunneling probability through the classically forbidden region is $t = e^{-\int_{r_i}^{r_o} |p_r^2| dr/h}$ [14].

Despite the strong interplay between electron core and hole shell across the n-p junction, we show that the energy of the electron-core states can be calculated separately by taking into account a tunneling dependent reflection phase θ at the n-p junction. The processing orbits for electron in the center-symmetric field yields a two-valued momentum field $q(r)$ (a two-torus, Fig. 3(a)) between the two classical return points r_i' and r_i [16]. Following EBK rule, in this case the semiclassical quantization condition for the trapped electron in the CNPJ can be considered along the radial and azimuthal coordinates C_R and C_θ separately, $\oint_{C_R} p_r dr + \varphi_B^e|_R + \alpha + (-\frac{\pi}{2} + \theta) = 2\pi n$ and $\oint_{C_\theta} p_\theta dr + \varphi_B^e|_\theta = 2\pi m$, determining the radial and azimuthal quantum numbers (n, m) . For massless Dirac electrons on the TI surface, $\varphi_B^e|_\theta$ is always 1, yielding the half-integer value of m . The Berry's phase $\varphi_B^e|_R$, as has been discussed above, will switch from 0 to 1 at the critical condition [7]. Here $\alpha = -\frac{\pi}{2}$ is the reflection phase at the inner turning point r_i' [17]. The radial quantization condition is now reduced into

$$\oint_{C_R} p_r(r) dr = 2\pi \left[n + \frac{1}{2}(1 - \varphi_B^e|_R) \right] - \theta. \quad (2)$$

For the reflection phase θ at the n-p junction, we adopt the result of connection problem for a single n-p junction by WKB approximation [18,19], $\theta = \text{Arg}[\Gamma(1 + i\frac{K}{\pi\hbar})] - \frac{\pi}{4} + \frac{K}{\pi\hbar} - \frac{K}{\pi\hbar} \ln(\frac{K}{\pi\hbar})$, where $K = \int_{r_i}^{r_o} |p_r^2| dr$. Note that θ is thus a function of the tunneling probability $t = e^{-K/h}$. From Eqns. (1) and (2), the energy ε_{nm} for each state (n, m) at different magnetic field B can be obtained semiclassically [detailed in section II of Appendix B].

In Fig. 3(b), we compared the semiclassical results w/o the tunneling correction with the numerical ones for the $m = \pm 1/2$ states. The condition without tunneling (dashed) corresponds to the $\theta = 0$ case. The semiclassical results with tunneling correction (solid)

fit the numerical results much better, especially at low fields. Near the critical field at which Berry-phase switch happens, θ approaches $-\frac{\pi}{4}$ (dotted curves for $(0, 1/2)$), resulting in an upturn in energy to get larger radial actions compared with the $\theta = 0$ case. At fields well above the criticality B_c , θ approaches 0 and there is no difference between these two cases any more. In addition, each state with positive m intersects with B_c at two critical fields between which this state seems to disappear. Actually, in the critical region the electron-core and hole-shell merge into snake states (will be detailed elsewhere), which are mixture of electron and hole states [20,21]. Furthermore, here we see the discrepancy between the semiclassical and numerical data for the state $(0, 1/2)$. It comes from the fact that we treat the hole system as continuum, which is no longer true at high magnetic fields where the hole states become quantized. This discrepancy is large for electron states (n, m) whose energies are near the top energy of the hole shell, where the hole states become well quantized.

IV. THE EXPERIMENTAL FD STATES IN THE CNPJ OF TI SS

Figures 3(c) and 3(d) are the experimental field-dependent dI/dV spectra up to 8 T taken at $r = 0$ and 0.3 (in units of r^*) as well as the corresponding numerical data. The dashed line indicates the magnetic field of 1 T, below which the data shows Berry-phase switch behavior as reported [7]. The FD states gradually evolve from the electrostatic-confinement region into the Landau region with the increasing magnetic field, with $N = n + (|m - \frac{1}{2}| - (m - \frac{1}{2}))/2$ being the correspondence between the Landau level (LL) and FD indexes. For example, the 0-th LL is composed of the successive $(0, m)$ states, with the energies increasing with m . The numerical results of the FD states match well with the experimental ones. In addition, the results obtained by our semiclassical analysis follow the same trend as the numerical data. The most distinct signature of Dirac fermions in the FD spectrum compared with Schrödinger electrons is the LDOS at the junction center (Fig. 3(c)). Each n -th LL is composed of double FD states, $(n, +1/2)$ and $(n-1, -1/2)$, which comes from the spinor nature of Dirac Hamiltonian. The only exception is the zeroth LL which only has one component, the $(0, +1/2)$ state.

The correspondence between the FD and the LL indexes can be seen more explicitly

in the spatial profile of the confined states. In Fig. 4(a), the experimental data shows discrete FD states at various magnetic fields, most of which can be clearly indexed and in accord with the numerical data (Fig. 4(b)). The dotted curve in Fig. 4(b) denotes the $(0, m)$ states, while the dashed one is the spatial profile of Dirac points. At 8 T, the $(0, m)$ states are pinned at the Dirac energies, following a trend that mimics the potential profile. This is because the radial action (Eqn. 1) for the $(0, m)$ state switches from $\pi - \theta$ to $-\theta$ after the Berry-phase switch (φ_B^e switches from 0 to π), where θ approaches 0 with the increasing magnetic field. A near-zero radial action means that the state resides nearly at the bottom of the electron-core (classically allowed region of the electron states), which is exactly the critical point (Dirac energy at the n-p interface). This can be seen clearly in the e-h core-shell structures at high fields in Fig. 1(b). Thus, from the spatial profile of the successive $(0, m)$ states, the potential profile can be figured out. Figure 4(c) shows the dI/dV spectra at the center and at an off-center ($r = 0.3$) position. The 0-th LL is composed of the $(0, m = 1/2, 3/2, \dots)$ states. The spatial distribution of these states thus the landscape of the potential profile can be visualized by taking the dI/dV mapping (Fig. 4(d)) at the energies of these successive peaks.

At relatively high magnetic fields, compressible and incompressible regions will form in a 2D electron system with potential variation because of the formation of LLs and the increased electron-electron interaction. The screened potential profile of the subsurface charged defects will be modified in this case. In the numerical data, without taking into account the electron-electron interaction, the potential profile (profiled by the $(0, m = 1/2, 3/2, \dots)$ states) does not change. Experimentally, the potential profile at 14 T is steeper by 8 meV than that at 8 T. In addition, there are signatures of kinks (arrowed in Fig. 4(a)) in the potential profile, which indicate the reduced screening as well as the formation of incompressible regions at relatively high magnetic fields. Compared with the graphene case [22], the kinks are very weak and no charging effect can be observed probably because of the strong screening from the bulk states or there are relaxation channels to the bulk states for the localized LL electrons.

V. CONCLUSIONS

We analyze the FD states in a CNPJ of TI SS with a confining potential that is typical

of the screened sub-surface charged defects. Unlike the FD states in conventional platforms as well as those of Dirac systems but in different confining potentials, the trapped electrons and holes show a unique electron-hole core-shell structure. There is strong interplay between the e-core and the h-shell because of the Klein tunneling, which can be modeled semiclassically to accurately simulate the electron-core states and the related exotic behaviors related to the interplay between them. This is accomplished by employing an energy, magnetic-field and angular-momentum dependent phase term θ coming from Klein tunneling across the n-p junction. Experimentally, the FD states are obtained up to 14 T, directly visualizing distinct nature of Dirac fermions as well as the potential profiles at different magnetic fields. The potential profiles at higher magnetic fields are found to be deformed compared with those at low fields, indicating the reduced screening of the topological surface states and stronger electron-electron interaction therein. The unique core-shell structure of the CNPJ might yield the high tunability of the coupling between them when constructed into CNPJ arrays. Our work indicates that the surface of a 3D TI, when tuned near the charge neutrality condition [23], offers an ideal platform to explore rich physics of the 2D Dirac fermion system, such as electron optics and quantum information technologies, etc.

ACKNOWLEDGEMENT

The authors acknowledge the supporting from National Science Foundation of China (Grants No. 61804056, 92065102, 2022YFA1403100).

APPENDIX A: EXPERIMENTAL DETAILS ON THE PREPARATION OF TOPOLOGICAL CNPJ

In this appendix, we show the technical details which are not important for our discussion but might be useful for the readers to reproduce the results.

All the experiments were carried out at 5.6 K in a low temperature scanning tunneling microscope (Unisoku) equipped with a 15 T magnet. The dI/dV (scanning tunneling spectroscopy) is taken with a modulation voltage of 1 meV (2 meV, peak to peak) at 987.5 Hz.

The 7-QL Sb_2Te_3 film was grown by molecular beam epitaxy on the $SrTiO_3$ (111) substrate. The Sb_2Te_3 films are usually heavily p-doped [21]. The $SrTiO_3$ (STO) substrate has a strong n-doping effect on the Sb_2Te_3 films. By minimizing the p-type defects in Sb_2Te_3 , the Fermi level of the top surface states of the films can be effectively tuned across the bulk gap, covering both the p-type and n-type regions. The thickness of 7-QL was chosen based on two reasons. First, the film must be thin enough because the substrate's n-doping effect on the top surface decreases with the increasing thickness. Second, the film must be thick enough, otherwise the top and bottom surface states hybridize and open a gap. The Berry's phase is illly defined in this case. According to the literature, the hybridization is minimized already in the 4-QL films [15].

To obtain the circular n-p junctions in Sb_2Te_3 films, we prepared a slightly p-doped film. During the growth of the first QL, access Te atoms were introduced by increasing the flux of Te and decreasing the substrate temperature, leading to the Te-on-Sb defects in the first QL only. These subsurface defects are positively charged, yielding electron puddles in the slightly p-doped top surface states.

In the manuscript, we investigate the same CNPJ as that in our previous work [7]. Here we use the length scale $R_0 = 50$ nm instead of 60 nm to give the best fitting to the field-dependent data for the $(0, \pm 1/2)$, $(1, \pm 1/2)$ states with low n (Fig. 3).

APPENDIX B: TECHNICAL DETAILS OF SEMICLASSICAL AND NUMERICAL CALCULATIONS

1. Details of the semiclassical calculation of the trapped FD states

In the semiclassical calculation of the FD states (magnetic-field dependent energy) shown in Fig. 3, we use Eqns. (1) and (2) as well as $\theta = Arg[\Gamma(1 + i\frac{K}{\pi h})] - \frac{\pi}{4} + \frac{K}{\pi h} - \frac{K}{\pi h} \ln(\frac{K}{\pi h})$. Here $K = \int_{r_i}^{r_o} |p_r^2| dr$. Note that for trapped electron states, $p_r = +\sqrt{(\varepsilon - U)^2 - (m/r - Br/2)^2}$. In Eqn. (2) of $\oint_{C_R} p_r(r) dr = 2\pi[n + \frac{1}{2}(1 - \varphi_B^e|_R)] - \theta$, $\varphi_B^e|_R$ is 0 (1) before (after) the Berry-phase switch. The critical field $B_c(\varepsilon)$ is obtained by the condition $q_r = q_\theta = 0$ (in this case the electron approaches the classical turning point r_i with a zero azimuthal momentum q_θ so that r_i and r_o coincide and there is no tunneling barrier any more) as mentioned in the main text. In this critical condition, the electron approaches the classical turning point r_i with a zero azimuthal momentum q_θ . In this case r_i and r_o coincide, so that there is no tunneling barrier any more.

The action J for a closed loop along C_R $\oint_{C_R} p_r(r) dr = \int_{r_i}^{r_o} p_r(r) dr + \int_{r_o}^{r_i} p_r(r) dr$. For a specific (n, m) electron states in a magnetic field of B in the CNPJ, the action is a function of the energy ε and monotonically increases with ε . Note that the classical turning points r_o, r_i are obtained from $p_r(\varepsilon, r) = 0$ and are also depend on the energy ε . Hence, we have the radial action

$$J(\varepsilon) = \int_{r_i(\varepsilon)}^{r_o(\varepsilon)} p_r(\varepsilon, r) dr + \int_{r_o(\varepsilon)}^{r_i(\varepsilon)} p_r(\varepsilon, r) dr = 2\pi[n + \frac{1}{2}(1 - \varphi_B^e|_R)] - \theta(\varepsilon) \quad (3)$$

for specific n, m, B , by which we can thus obtain the energy $\varepsilon(n, m, B)$ that satisfies this equation by the iterative method.

Figure 5 takes the $(0, 1/2)$ state as an example. The upper and lower solid curves are the energy ε that satisfies Eqn. (3) for $n = 0, m = 1/2$ at different magnetic fields B with $\varphi_B^e|_R$ equals 0 and 1, respectively. The dashed curve is the critical condition for the Berry's phase, which means that the curve defines the boundary between the states with $\varphi_B^e|_R = 0$ (shadowed region) and those with $\varphi_B^e|_R = 1$. The two crossing points between the two $\varepsilon(B)$ curves and the B_c curve define the two critical field B_{c1} and B_{c2} for the $(0, 1/2)$ states. This means that the Berry-phase switch doesn't happen abruptly and there appears a transient region between B_{c1} and B_{c2} between which the electron state $(0, 1/2)$ seems disappear. Actually, the e-core and h-shell merge together to form

snake states (mixture of electron and hole states) in such case and will be detailed elsewhere.

Thus, by taking the upper curve below B_{c1} and the lower curve above B_{c2} , the semiclassical data for $(0, 1/2)$ is obtained as has been plotted in Fig. 3.

2. Details of the numerical calculation of the LPDOS

In the presence of a rotational symmetric field $U(r)$ for the circular n-p dot of the surface states, the Dirac equation in the main text can be solved by the radial equation

$$\begin{pmatrix} U(r) - \varepsilon & \partial_r + m/r - Br/2 \\ -\partial_r + m/r - Br/2 & U(r) - \varepsilon \end{pmatrix} \begin{pmatrix} u_1 \\ u_2 \end{pmatrix} = 0 \quad (4)$$

by using the eigenstates for Eq. S1 in the form of

$$\Psi_m(r, \theta) = \frac{e^{im\theta}}{\sqrt{r}} \begin{pmatrix} u_1(r)e^{-i\theta/2} \\ u_2(r)e^{i\theta/2} \end{pmatrix}. \quad (5)$$

We solve the radial equation (4) by the finite-difference method by using a system size $L = 20$ and the number of sites $N = 2000$. In the numerical data of Fig. 2, we use an energy broadening of $2\pi/L$ caused by the finite system size of L , which corresponds to an energy broadening of about 1.2 meV. In the numerical data of Fig. 3 and Fig. 4, we use an energy broadening of $0.5\varepsilon^*$ (~ 2 meV) to give the best fitting to the experimental data.

APPENDIX C: THE CORE-SHELL STRUCTURE OF FD STATES IN A CNPJ OF TI SS FOR $m = 1/2$

In Fig. 6, the classical allowed regions, the LPDOS along the radial direction at 0 T and 0.18 T, the field dependent LPDOS at the center position obtained numerically for the $m = 1/2$ states are show in comparison with those for the $m = 7/2$ states in the main text.

For the $m = 1/2$ states, the interplay between the e-core and h-shell is much more sensitive to the magnetic field. As shown in Fig. 6(a) and (c), the critical point reaches nearly the same energy (near $(2, 7/2)$) at 0.18 T as that (near $(2, 1/2)$) at 1 T for the $m = 7/2$ states in Fig. 2(b). For both states, in the intermediate magnetic field region (centered around the critical field B_c) the electron energy levels at the junction center are the envelope of the hole levels.

REFERENCES

- [1] M. Z. Hasan and C. L. Kane, *Colloquium : Topological Insulators*. Rev. Mod. Phys. **82**, 3045 (2010).
- [2] X.-L. Qi and S.-C. Zhang, *Topological Insulators and Superconductors*. Rev. Mod. Phys. **83**, 1057 (2011).
- [3] V. V. Cheianov, V. Fal'ko, and B. L. Altshuler, *The Focusing of Electron Flow and a Veselago Lens in Graphene P-N Junctions*. Science **315**, 1252 (2007).
- [4] S. Chen, Z. Han, M. M. Elahi, K. M. M. Habib, L. Wang, B. Wen, Y. Gao, T. Taniguchi, K. Watanabe, J. Hone *et al.*, *Electron Optics with P-N Junctions in Ballistic Graphene*. Science **353**, 1522 (2016).
- [5] M. I. Katsnelson, K. S. Novoselov, and A. K. Geim, *Chiral Tunnelling and the Klein Paradox In graphene*. Nat. Phys. **2**, 620 (2006).
- [6] M. Chen, Y.-P. Jiang, J. Peng, H. Zhang, C.-Z. Chang, X. Feng, Z. Fu, F. Zheng, P. Zhang, L. Wang *et al.*, *Selective Trapping of Hexagonally Warped Topological Surface States in a Triangular Quantum Corral*. Sci. Adv. **5**, eaaw3988 (2019).
- [7] J. Zhang, Y.-P. Jiang, X.-C. Ma, and Q.-K. Xue, *Berry-Phase Switch in Electrostatically Confined Topological Surface States*. Phys. Rev. Lett. **128**, 126402 (2022).
- [8] Y. Zhao, J. Wyrick, F. D. Natterer, J. F. Rodriguez-Nieva, C. Lewandowski, K. Watanabe, T. Taniguchi, L. S. Levitov, N. B. Zhitenev, and J. A. Stroscio, *Creating and Probing Electron Whispering-Gallery Modes in Graphene*. Science **348**, 672 (2015).
- [9] J. Lee, D. Wong, J. Velasco Jr, J. F. Rodriguez-Nieva, S. Kahn, H.-Z. Tsai, T. Taniguchi, K. Watanabe, A. Zettl, F. Wang *et al.*, *Imaging Electrostatically Confined Dirac Fermions in Graphene Quantum Dots*. Nat. Phys. **12**, 1032 (2016).
- [10] C. Gutiérrez, L. Brown, C.-J. Kim, J. Park, and A. N. Pasupathy, *Klein Tunnelling and Electron Trapping in Nanometre-Scale Graphene Quantum Dots*. Nat. Phys. **12**, 1069 (2016).
- [11] S.-Y. Li and L. He, *Recent Progresses of Quantum Confinement in Graphene Quantum Dots*. Frontiers of Physics **17**, 33201 (2021).
- [12] V. V. Cheianov and V. I. Fal'ko, *Selective Transmission of Dirac Electrons and Ballistic Magnetoresistance of N-P Junctions in Graphene*. Phys. Rev. B **74**, 041403 (2006).
- [13] S. M. Reimann and M. Manninen, *Electronic Structure of Quantum Dots*. Rev. Mod. Phys. **74**, 1283 (2002).
- [14] H.-Y. Chen, V. Apalkov, and T. Chakraborty, *Fock-Darwin States of Dirac Electrons in Graphene-Based Artificial Atoms*. Phys. Rev. Lett. **98**, 186803 (2007).
- [15] Y. Jiang, Y. Wang, M. Chen, Z. Li, C. Song, K. He, L. Wang, X. Chen, X. Ma, and Q.-K. Xue, *Landau Quantization and the Thickness Limit of Topological Insulator Thin Films of Sb₂Te₃*. Phys. Rev. Lett. **108**, 016401 (2012).
- [16] A. D. Stone, *Einstein's Unknown Insight and the Problem of Quantizing Chaos*. Phys. Today **58**, 37 (2005).
- [17] D. J. W. Geldart and D. Kiang, *Bohr-Sommerfeld, Wkb, and Modified Semiclassical Quantization Rules*. American Journal of Physics **54**, 131 (1986).
- [18] M. V. Berry and K. E. Mount, *Semiclassical Approximations in Wave Mechanics*. Reports on Progress in Physics **35**, 315 (1972).
- [19] T. Tudorovskiy, K. J. A. Reijnders, and M. I. Katsnelson, *Chiral Tunneling in Single-Layer and Bilayer Graphene*. Phys. Scr. **2012**, 014010 (2012).
- [20] C. W. J. Beenakker, *Colloquium: Andreev Reflection and Klein Tunneling in Graphene*. Rev. Mod. Phys. **80**, 1337 (2008).

- [21] P. Carmier, C. Lewenkopf, and D. Ullmo, *Graphene N-P Junction in a Strong Magnetic Field: A Semiclassical Study*. Phys. Rev. B **81**, 241406 (2010).
- [22] C. Gutiérrez, D. Walkup, F. Ghahari, C. Lewandowski, J. F. Rodriguez-Nieva, K. Watanabe, T. Taniguchi, L. S. Levitov, N. B. Zhitenev, and J. A. Stroscio, *Interaction-Driven Quantum Hall Wedding Cake-Like Structures in Graphene Quantum Dots*. Science **361**, 789 (2018).
- [23] Y. Jiang, Y. Y. Sun, M. Chen, Y. Wang, Z. Li, C. Song, K. He, L. Wang, X. Chen, Q.-K. Xue *et al.*, *Fermi-Level Tuning of Epitaxial Sb₂Te₃ Thin Films on Graphene by Regulating Intrinsic Defects and Substrate Transfer Doping*. Phys. Rev. Lett. **108**, 066809 (2012).

Figure Captions

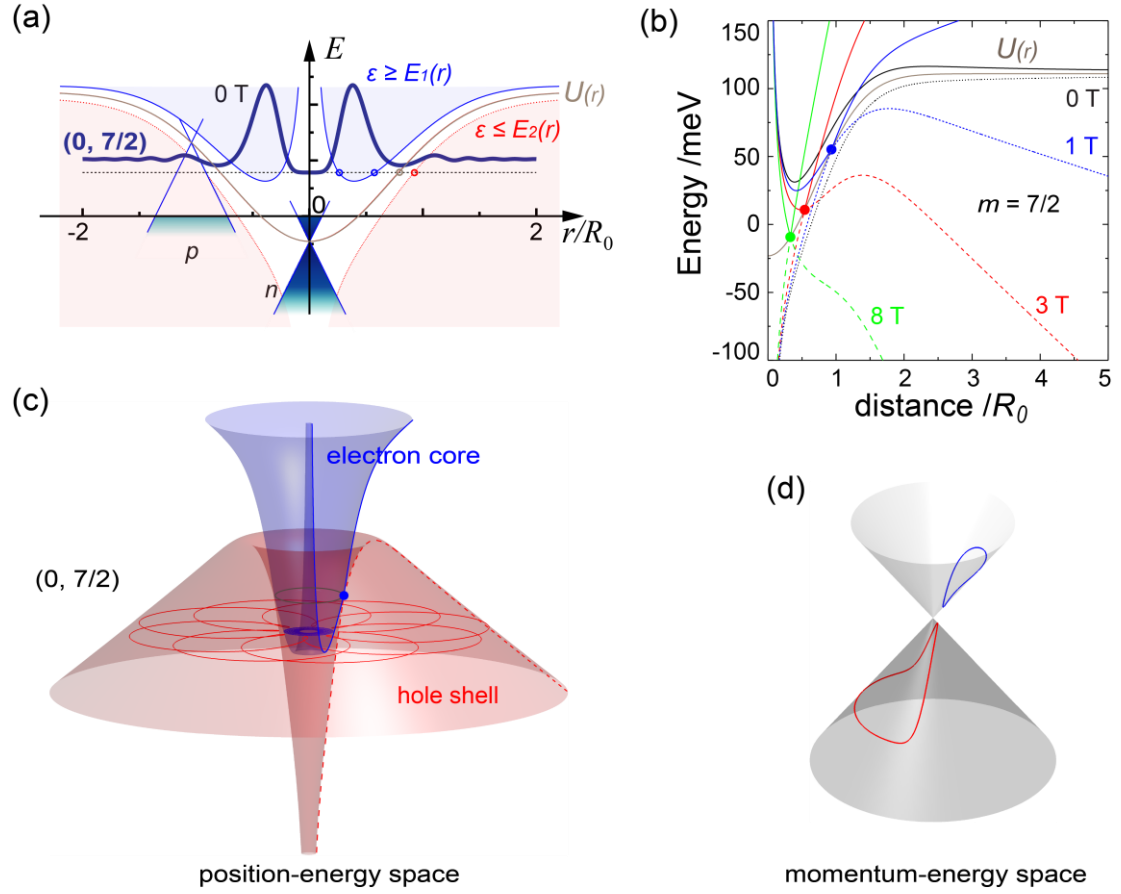


FIG. 1 (color online). The electron-hole (e-h) core-shell structure of the FD states in a CNPJ of TI SS. (a) The potential profile $U(r)$ (gray curve) of the CNPJ in the radial direction. The classical allowed region for electrons and holes at 0 T is also plotted for the $m = 7/2$ states. The thick-solid curve is the radial profile (numerical) of the $(0, 7/2)$ states with its energy indicated by the horizontal dashed line. The hollow dots are the classical turning points. (b) Field-dependence of the e-h core-shell structures for $m = 7/2$. The solid and dashed curves indicate the region boundaries for electrons and holes. The solid dots denote the touch points in the e-h core-shell structures at different magnetic fields. (c) The 3D view of the core-shell structure in the position-energy space for $m = 7/2$ states at 1 T as well as the classical electron and hole orbits for $(0, 7/2)$. The solid dot and the circle indicate the touching between electron and hole regions. (d) The electron and hole orbits for $(0, 7/2)$ in the momentum-energy space. The spatial and radial profiles (numerical) of the trapped $(0, 7/2)$ state at 0 T and 1 T. In the simulation, we use a radial length scale $R_0 = 50$ nm, a Fermi velocity $v_F \sim 4.3 \times 10^5$ m/s² and the

confining potential $U(r) = \mu_0 e^{-r^2} + \mu_\infty$. Here $\mu_0 = -34.2\varepsilon^*$, $\mu_\infty = 28.4\varepsilon^*$, energy scale $\varepsilon^* = \hbar v_F / R_0 \sim 3.91$ meV. We use the convention that the states with positive m show Berry-phase switch in positive B .

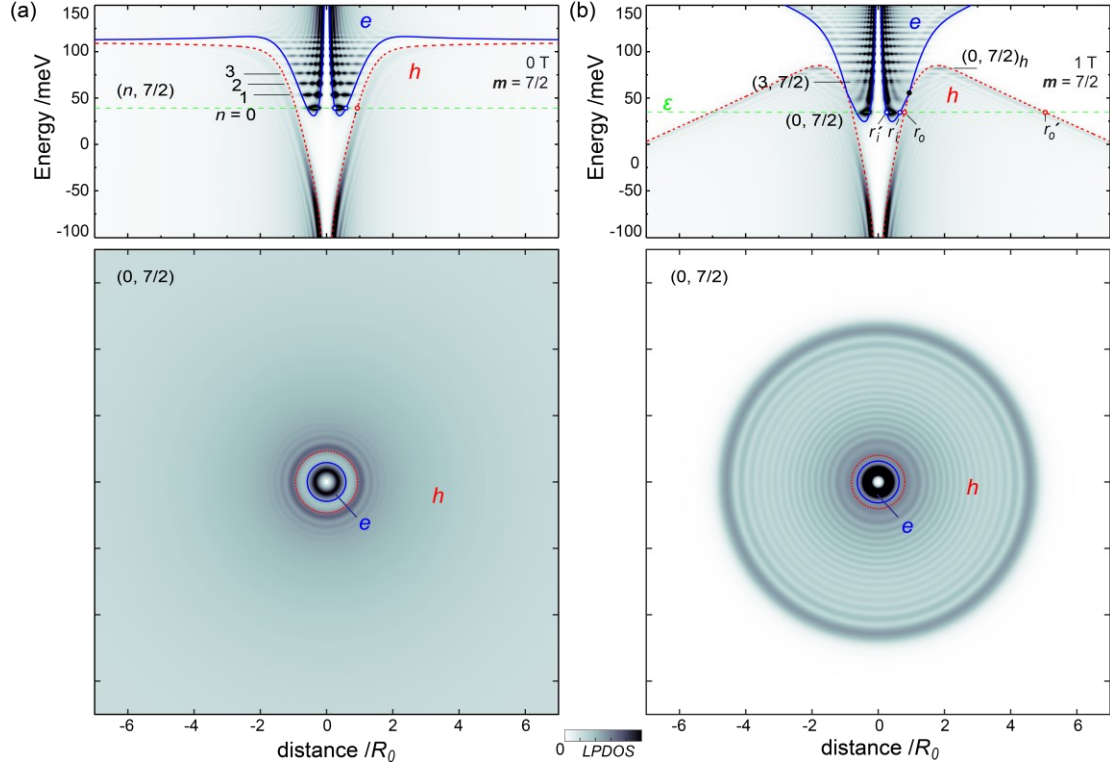


FIG. 2 (color online). The numerical e-h core-shell structure. (a) (b) The LPDOS ($m = 7/2$, numerical) along C_R (upper ones) as well as the spatial distribution of the state $(0, 7/2)$ at 0 T and 1 T, respectively. The energies of $(0, 7/2)$ are indicated by the dashed horizontal lines. The classical boundaries for the e-h core-shell structures are also plotted. The solid and dashed circles in the lower figures denote the classical forbidden regions. Here $(0, 7/2)_h$ denotes the topmost one of the quantized hole states.

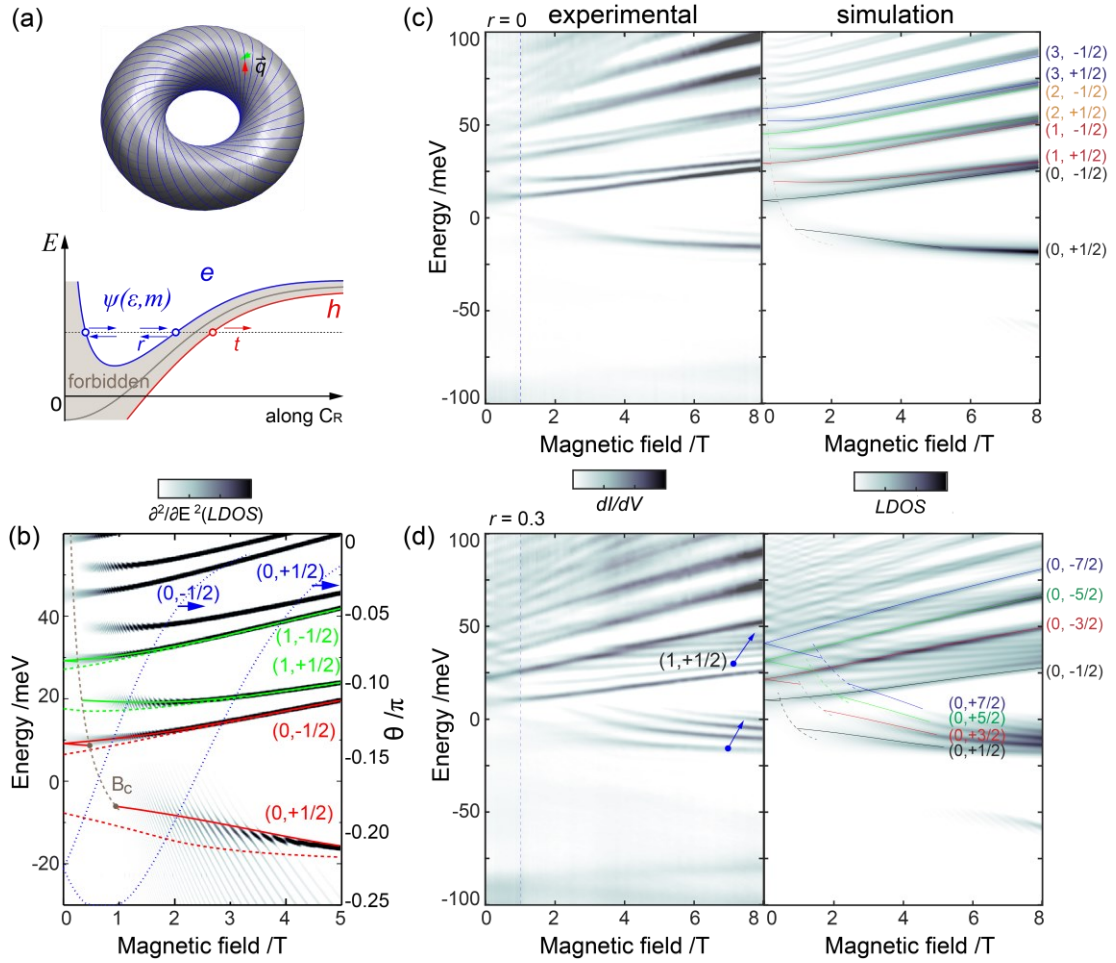


FIG. 3 (color online). Field-dependent FD states obtained semiclassically, numerically and experimentally. (a) The vector field for the electron states of $(0, 7/2)$ at 0 T as well as the diagram of tunneling between the electron core and hole shell at the n-p junction. (b) The comparison between the FD states $(0, \pm 1/2)$, $(1, \pm 1/2)$ obtained numerically (second differentiated, color map) and semiclassically. Here we show both the semiclassical results with (solid curves) and without (dashed curves) the tunneling correction. The blue dotted curves are the $\theta(B)$ for $(0, \pm 1/2)$. (c) (d) The experimental FD states obtained at the center and an off-center position in the CNPJ as well as the corresponding numerical data. The dashed lines indicate the region of $[0, 1]$ T where Berry-phase switch behaviors can be observed [7]. The semiclassical data (solid curves) by the modified EBK rule is plotted along with FD states obtained numerically. The dashed curves are $B_c(\varepsilon)$ for the states with different m . All the experimental data are taken at 5.6 K.

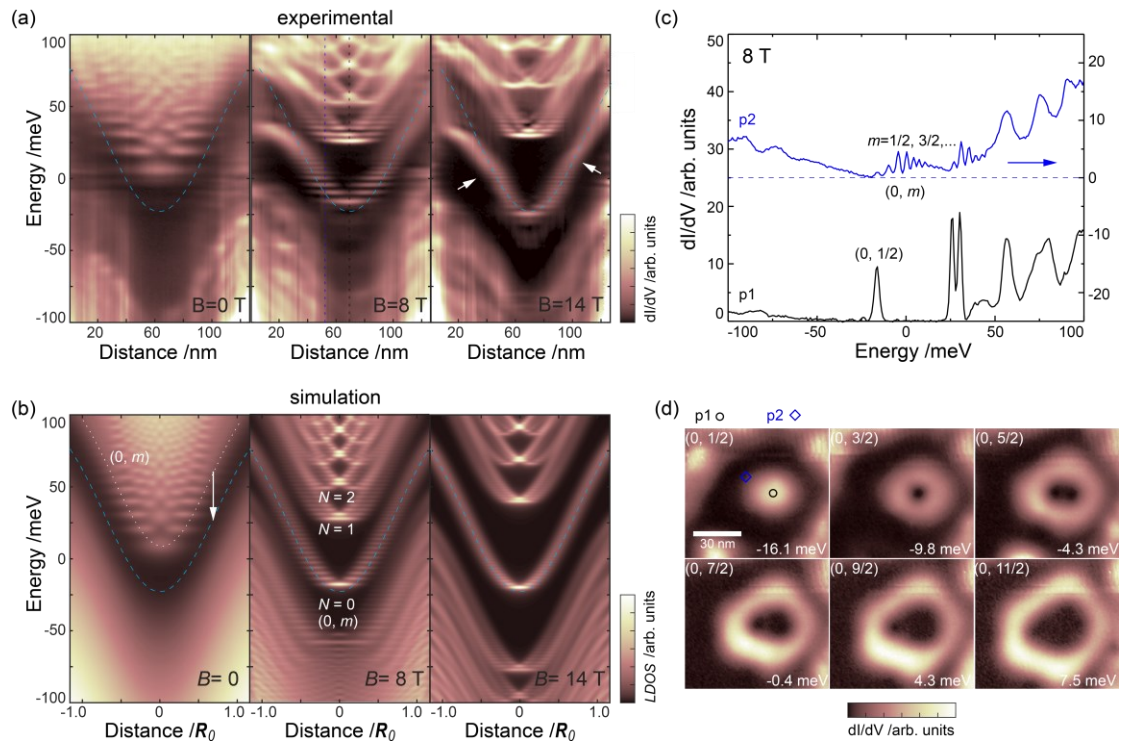


FIG. 4 (color online). The spatial profiles of the FD states at various magnetic fields. (a) (b) The spatially resolved dI/dV and the corresponding numerical results long a line (126 data points, 125 nm) across the CNPJ at 0 T, 8 T and 14 T, respectively. The dotted line indicates the $(0, m)$ states at 0 T. The dashed curves are the potential profiles. (c) The dI/dV taken at two different positions (indicated in (d)) in the CNPJ. (d) The dI/dV mapping taken at energies corresponding to those of the $(0, m)$ states at 8 T.

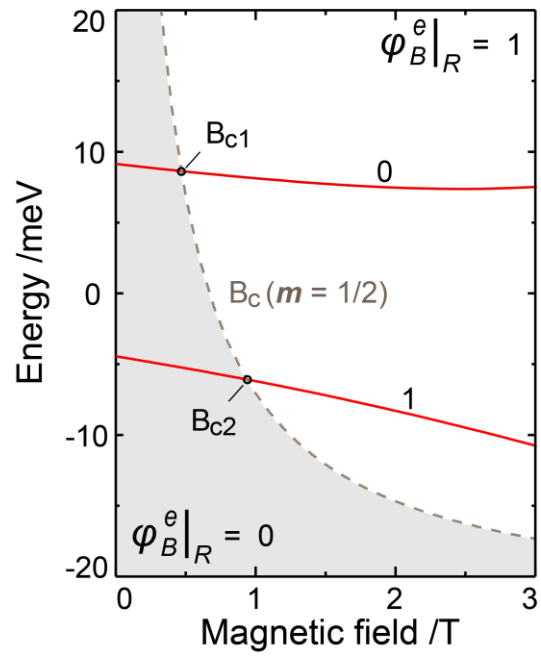


FIG. 5 (color online). The energy of the state $(0, 1/2)$ obtained semiclassically by Eqn. (3) with $\varphi_B^e|_R = 1$ and 0 , respectively. The dashed line is the B_c for $m = 1/2$.

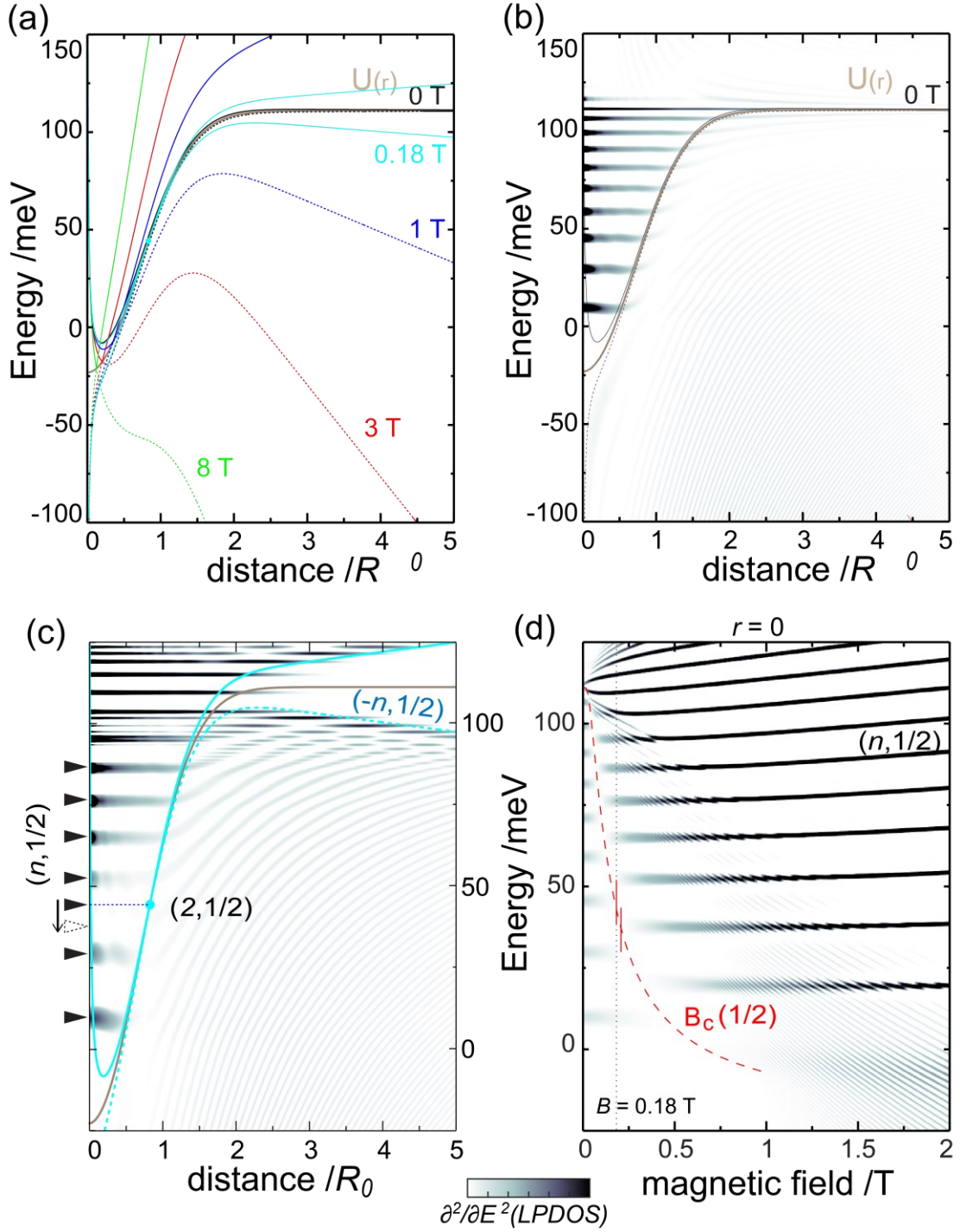


FIG. 6 (color online). The core-shell structure of FD states in a CNPQD of TI SS for $m = 1/2$. (a) The classical allowed regions for electrons (solid curves) and holes (dashed curves) at 0 T, 1 T, 3 T and 8 T for $m = 1/2$. The cyan solid dot indicates the critical point where there is no barrier for the tunneling between electron and hole states at 0.18 T. Here the 2nd differentiated LPDOS ($m = 1/2$, numerical) at 0 T and 0.18 T are also shown in (b) and (c). The field of 0.18 T is the critical condition for the Berry-phase

switch for the state $(2, 1/2)$. (d) The second differentiated LPDOS ($m = 7/2$, numerical) plotted along with the classical allowed region at 1 T in a smaller energy range. (f) The 2nd differentiated LPDOS ($m = 1/2$, $r = 0$, numerical) as a function of the magnetic field B up to 2 T. The dotted line indicates the magnetic field of $B = 0.18$ T. The dashed curve is B_c ($m = 1/2$).